ADVANCED MATERIALS
www.advmat.de

# Massively Scalable Self-Assembly of Nano and Microparticle Monolayers via Aerosol Assisted Deposition

*Gabriel Cossio, Raul Barbosa, Brian Korgel, and Edward T. Yu**

**An extremely rapid process for self-assembling well-ordered, nano, and microparticle monolayers via a novel aerosolized method is presented. The novel technique can reach monolayer self-assembly rates as high as 268 $cm^2$ $min^{-1}$ from a single aerosolizing source and methods to reach faster monolayer self-assembly rates are outlined. A new physical mechanism describing the self-assembly process is presented and new insights enabling high-efficiency nanoparticle monolayer self-assembly are developed. In addition, well-ordered monolayer arrays from particles of various sizes, surface functionality, and materials are fabricated. This new technique enables a 93× increase in monolayer self-assembly rates compared to the current state of the art and has the potential to provide an extremely low-cost option for submicron nanomanufacturing.**

## 1. Introduction

The ability to engineer matter at the nanometer and submicron scale has become increasingly important for the development of next generation nanophotonic, biomedical, renewable energy, and semiconductor technologies.[1–5] Currently, many developing technologies require periodic submicron surface patterning, and often the need for extreme patterning resolution and fidelity can be relaxed to only local ordering. For example, quasi-random submicron sized scattering structures can enable III-V photovoltaics (PVs) to maintain high power conversion efficiency while decreasing absorber thickness by maintaining light trapping resonances with high spectral density and broadband operation.[6] These advancements have enabled extremely high specific power (W $kg^{-1}$) and are very important for improving market competitiveness and widening the scope of PV power generation to new areas such as the automotive industry, unmanned aerial vehicles, and building integrated PVs.[1,7–9] Similarly, periodic arrays of dielectric, semiconductor, and plasmonic nanostructures have also demonstrated powerful sensing[2,3,10,11] and catalytic capabilities[4,5,12] as well as antireflection,[13–16] structural coloring[17–22] properties, and have successfully been used to fabricate high-quality transparent electrodes[23,24] which are important for next generation display, public health, and aerospace technologies. Currently, the submicron nanostructures enabling these technologies are made utilizing nanoimprint lithography, electron beam lithography, or photolithography. While these platforms offer high repeatability, precision, and pattern fidelity, they require massive capital investments preventing their use for the manufacturing of low-cost technologies.

Since Deckman and Van Duyne's seminal works,[25–27] monolayer arrays of colloidal polymeric micro and nanoparticles (NPs) have been extensively investigated for use as low-cost submicron lithographic templates. Leveraging NPs as lithographic masks can enable extremely low cost nanopatterning due to its parallelized self-assembled nature, wide particle size availability (10′s–1000′s nm), and the extremely low-cost synthesis of colloidal NPs. For example, a 2.5 mL solution of 100 nm diameter polystyrene (PS) NPs (5 wt%) can form a hexagonally close packed NP monolayer pattern over a 1 $m^2$ area. Based on current typical prices of chemical precursors used in the experiments reported here, we can estimate material costs in the \$0.01 $cm^{-2}$ range. While colloidal lithography has seen broad use since its development, with only a few exception[28,29] it has been plagued by poor scaling which has limited its use to research-scale devices with $cm^2$ footprints or smaller.[30–32] The inability to scale colloidal lithography has greatly constrained the usefulness of the technique and limited its application to academic research and device prototyping.

Over the years, various techniques have been developed to increase the throughput of colloidal lithography, including spin coating,[33] convective assembly and blade coating,[34–36] and Langmuir–Blodgett (LB) based methods.[28,29,37–40] While many of these techniques have been leveraged to self-assemble high quality and large-area NP monolayers, they suffer from either complex implementation[28] or slow monolayer self-assembly rates[29] ($mm^2$ $min^{-1}$) which has prevented their use in any commercial scale manufacturing. In order to unlock colloidal lithography's potential for low-cost submicron lithography a new self-assembly method must be developed that can rapidly create high quality

G. Cossio, E. T. Yu
Microelectronics Research Center
University of Texas at Austin
Chandra Department of Electrical and Computer Engineering
Austin, TX 78758, USA
E-mail: ety@ece.utexas.edu
R. Barbosa, B. Korgel
McKetta Department of Chemical Engineering
University of Texas at Austin
Austin, TX 78712, USA

The ORCID identification number(s) for the author(s) of this article can be found under https://doi.org/10.1002/adma.202309775

DOI: 10.1002/adma.202309775

 

and large-area NP monolayers and that easily integrates into existing manufacturing processes.

Here we present a new method for self-assembling NP monolayers on an air–water interface with massively improved monolayer self-assembly rates and throughput. We show that aerosolized NP suspensions can be utilized to self-assemble submicron NP monolayers at rates >93× higher than previous reports.[28] We additionally show that the surface properties of colloidal particles are critically important for increasing self-assembly rates and efficiency, and improving monolayer crystallinity. The methods described in this paper are highly modular, employ equipment currently utilized in commercial manufacturing, and do not require additional components commonly used in NP monolayer self-assembly to ensure high crystallinity NP monolayers (e.g., compressive barriers, surface tension sensors, and Brewster angle metrology).[32,34,41] Additionally, this methods compatibility with nonplanar substrates is also demonstrated, which is important for extending the technology's scope of use and meeting the lithographic needs of next-generation flexible devices. Lastly, we demonstrate that NPs which ordinarily are challenging to self-assemble at an air–water interface can be made to efficiently self-assemble by tailoring the NP surface properties. This new technique enables massively improved throughput of submicron NP self-assembly capabilities and has the potential to provide an affordable option for submicron nanomanufacturing.

Lastly, it is important to clarify that this manuscript details experiments with highly monodisperse and spherical particles in the 200–1000 nm diameter range. Therefore, the behavior of anisotropic and/or truly nanoscale (1–100 nm size range) colloidal particles may not necessarily follow the same diffusion and self-assembly characteristics as described in this work. As such, the compatibility of anisotropic and particles in the 1–100 nm size range will require additional experimental validation.

## 2. Results and Discussion

The LB technique[31,32] is the most widely used method to create ordered NP monolayers at an air–liquid interface. Generally, the particles of interest are suspended in a spreading agent (often a low surface tension alcohol when employing an air–water interface) that is continuously introduced onto the liquid surface in millimeter sized droplets. Impinging particles then spread across and remain trapped at the liquid surface due to the minimization of free energy. When the alcohol droplet impinges on the water surface a surface tension gradient is formed between the low surface tension alcohol and the high surface tension bulk water volume via the Marangoni force. This repulsive force causes mass flow along the water's surface and distributes the NPs radially away from the impinging site.[42] The number of NPs trapped on the water surface gradually increases, and these can be eventually self-assembled into ordered NP monolayers by careful optimization of the surface pressure via externally controlled compressive barriers. LB methods have been very successful in creating low-defect and large-area NP monolayers; however, the self-assembly of NP monolayers via LB methods is very slow ($mm^2\ min^{-1}$) and requires careful implementation of various methodologies to ensure low-defect self-assembly of NP monolayers.[29] The slow and sensitive nature of LB and other NP monolayer self-assembly techniques has greatly limited their throughput and prevented their widespread use.

In this work, we use a novel technique inspired by LB techniques and aerosolized jet printing. Aerosolized jet printing is a manufacturing process that has been used to synthesize microparticles, deposit low volume coatings, and print various inks with extremely high spatial resolution, repeatability, and great design flexibility.[43–47] To our knowledge, this technique has not been utilized to create NP monolayers via self-assembly. By aerosolizing the NP solution and optimizing interparticle interactions we demonstrate massive improvements to monolayer self-assembly rates and efficiency, while maintaining highly ordered NP monolayers. **Figure 1** depicts the atomization process and self-assembly of NP monolayers on an air–water interface utilized in this work. High frequency-oscillation (120 kHz) is used to create the finely atomized aerosol of aqueous ethanol into droplets, 15–25 μm in diameter, which are then focused into a collimated beam via pressurized air (Figure 1a). Colloidal NPs suspended in an aqueous ethanol solution (1:1 ethanol/water) are continuously pumped to the atomization nozzle via a computer-controlled syringe pump (Figure 1b).

The micron-sized droplets generated by the atomizing nozzle are a departure from the conventional millimeter sized droplets used in traditional LB systems. Previous work has shown that falling millimeter sized droplets generate large subsurface vortices which mix the droplet into the bulk water volume within times on the order of milliseconds.[48–50] This mixing action greatly limits the efficient transfer of microparticles to the air–water interface and may contribute to the low self-assembly speeds and efficiency of traditional LB methods. Instead, by suspending NPs in micron-sized alcohol droplets their kinetic energy can be reduced proportionally to their volume (roughly six orders of magnitude reduction relative to mm sized droplets). The large decrease in kinetic energy prevents the droplet from rupturing the air–water interface and greatly decreases mixing and the subsequent loss of NPs to the bulk water volume (Figure S1, Supporting Information). Additionally, it has been shown that due to solvent evaporation, micron scale aqueous ethanol droplets can shrink to 60% of their original size after 1 s of free fall.[51] The decrease in size from evaporation may further increase the transfer efficiency of NPs to the air–water interface.

After the atomized droplets strike the liquid interface, the Marangoni force propels NPs radially away from the atomized beam, which prevents NP aggregation at the site of injection (Figure 1c). We observe that the radially symmetric spreading of NPs away from the atomized beams enables the time-dependent self-assembly of a NP annulus. The continuous introduction of NPs via the aerosolized beam adds new NPs to the established annulus, causing it to thicken inwards from the outside perimeter of the containing reservoir toward the injection site until the annulus closes (Figure 1c). A real time video of the aerosolized self-assembly is presented in Video S1 (Supporting Information).

To understand the physical mechanisms enabling the improved NP self-assembly, we conducted a series of self-assembly experiments with varying NP flux ($\Phi$) and zeta potential ($\zeta$). Here we define $\Phi$ as the number of NPs impinging the liquid interface per unit time: $\Phi = n_{np} V_{fluid}$, where $n_{np}$ is the concentration of NPs in the dispensing solution in NPs $mL^{-1}$ and $V_{fluid}$ is the liquid delivery rate to the atomizing nozzle in mL $min^{-1}$. The

 

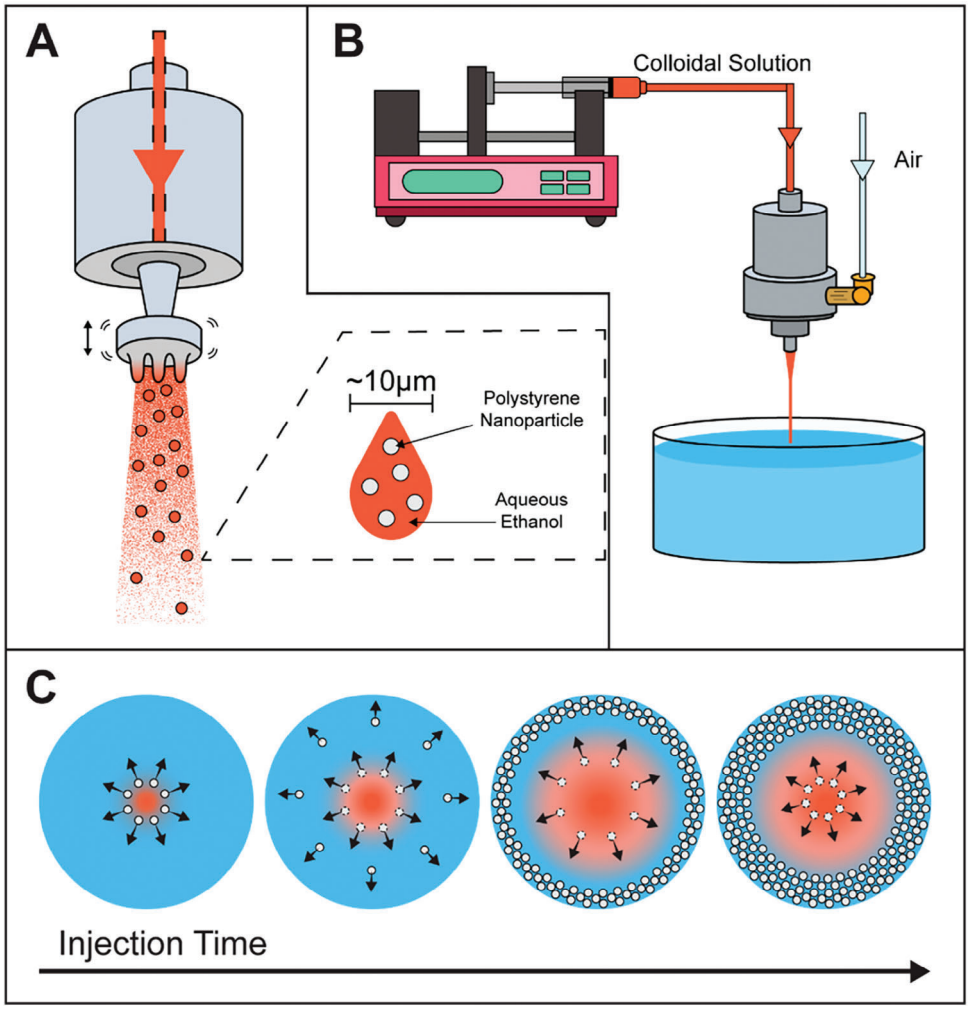


**Figure 1.** a) Schematic diagram of aerosolizing nozzle generating micron-scale dispensing droplets carrying submicron colloidal particles. b) Schematic diagram of monolayer self-assembly system. c) Process flow showing self-assembly of submicron colloidal particles self-assembling at an air–water interface as a function of injection time. (Left) Atomized droplets of aqueous alcohol dispensing droplets (orange) impinge on the water's surface (blue). The alcohol generates a surface tension gradient (orange) which propels submicron colloidal particles (white) radially away from the impact point. Over time continuous injection causes submicron particles to accumulate into an annulus and self-assemble into an ordered monolayer (Right).

zeta potential is the electric potential at the slipping/shear plane of a colloid particle moving under an applied electric field and reflects the potential difference between the electric double layer of electrophoretically mobile particles and their suspending solvent. In past work, we have shown that $\zeta$ can greatly affect the efficiency of NP self-assembly and the quality of self-assembled NP monolayers.[13]

NP flux dependent self-assemblies were performed via two different methods. In Method 1 (**Figure 2**a), the NP concentration in the atomizing solution, $n_{np}$, was kept constant while $\Phi$ was varied by changing the liquid delivery rate, $V_{fluid}$. Additionally, the number of atomized droplets generated by the atomizing nozzle increases as $V_{fluid}$ is increased. Therefore, tests performed under Method 1 maintain a dilute concentration of NPs within dispensing droplets and minimize the interparticle interactions between NPs.

In Method 2 (Figure 2b), self-assembly of NP monolayers was performed by increasing the NP concentration, $n_{np}$, in the atomizing solution while the liquid delivery rate, $V_{fluid}$, was kept constant. Under Method 2 the number of dispensing droplets generated is kept constant while the number of NPs within each droplet increases. Using Method 2, we can determine if interparticle interactions affect the self-assembly of the NP monolayer, as such interactions should become more prominent as the concentration of NPs within a single dispensing droplet is increased. In all testing methods the zeta potential of NP solutions was modified by either adsorption (increases $|\zeta|$) or desorption (decreases $|\zeta|$) of anionic sodium dodecyl sulfate (SDS) surfactant molecules as described in Experimental Section and in earlier work.[13]

In order to accurately calculate the average monolayer self-assembly rate experimental methods were adapted from Menath et al.[52]—whose work defines the closing of the self-assembling NP annulus as the point of highest NP concentration and the largest self-assembled monolayer area. We reason that the time it takes the NP self-assembly to reach this event (the closing of the NP annulus) can be accurately compared between the

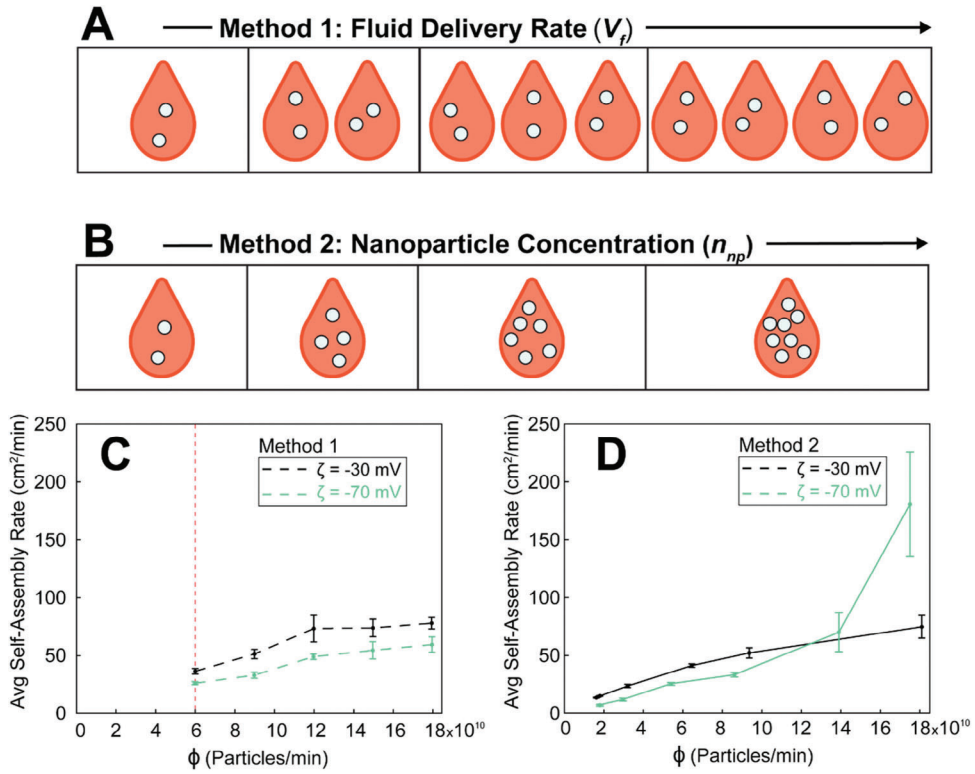


**Figure 2.** a) Diagram describing self-assembly Method 1. As the fluid delivery rate is increased ($V_f$) the atomizing nozzle creates a larger number of aqueous alcohol dispensing droplets (orange). The increasing fluid delivery rate also increases the flux of colloidal particles (white) leaving the nozzle. b) Diagram describing self-assembly Method 2. $V_f$ is not changed, therefore the number of aqueous dispensing particles is not varied. As the concentration of colloidal particles ($n_{np}$) is increased in dispensing solution, the number of nanoparticles (NPs) within the atomized aqueous alcohol dispensing particles increases. c) Zeta potential and NP flux dependent average monolayer self-assembly rates for monolayers prepared from 1 µm diameter polystyrene NPs via Method 1. Values of Φ to the left of the red dashed line did not sustain stable atomization. d) Zeta potential and NP flux dependent average monolayer self-assembly rates for monolayers prepared from 1 µm diameter polystyrene NPs via Method 2. Data points represent a minimum of $n = 5$ measurements for both (c) and (d).

different tested colloidal solutions. Therefore, the monolayer self-assembly rate is calculated as:

$$\text{Self-Assembly Rate} = \frac{A_{ML}}{t_{ML}} \quad (1)$$

where $A_{ML}$ is constant (169 cm$^2$) and is the final self-assembled monolayer area and $t_{ML}$ is the time until the annulus is fully closed. A total of five measurements are performed at each value of Φ.

For experiments performed via Method 1, NP concentrations of the dispensing solutions were maintained at $6 \times 10^{10}$ NPs mL$^{-1}$ and larger Φ was achieved by increasing $V_{fluid}$ from 0.10 to 0.15, 0.20, 0.25, and 0.30 mL min$^{-1}$. For experiments performed under Method 2, $V_{fluid}$ was maintained at 0.10 mL min$^{-1}$ while NP concentration was increased to attain larger Φ. It was not possible to maintain stable atomization for liquid dispensing rates below 0.10 mL min$^{-1}$. Results shown in Figure 2c,d were performed with 1 µm diameter PS NPs, 1.6 W nozzle power, 120 kHz nozzle frequency, a 40 mm spacing between the water and nozzle, and a 0.8 PSI focusing pressure. Each test was performed a minimum of five times. NP solutions with $|\zeta| = 30$ or 70 mV were tested.

Figure 2c shows the average NP monolayer self-assembly rate's dependence on Φ for monolayers prepared via Method 1. The dashed red line denotes values of Φ that were not accessible via Method 1 due to the lower limit of liquid dispensing rates. As shown, using Method 1 the average monolayer self-assembly rates are higher for NP solutions with a low $|\zeta|$ at all values of Φ, and average monolayer self-assembly rates increase linearly with Φ for both low and high $|\zeta|$ solutions. The higher $|\zeta|$ solutions have lower monolayer self-assembly rates because the NPs are more hydrophilic and are therefore more easily mixed into the bulk water volume. These findings are consistent with our previous reports detailing similar improvements in NP monolayer self-assembly rates using a needle injection method.[13] Additionally, these results demonstrate that the self-assembly rate of NP monolayers is simply proportional to the number of NPs being injected onto the surface when the atomized droplets contain a dilute concentration of NPs.

Figure 2d shows the results from tests performed under Method 2. As might be expected, the average monolayer self-assembly rate is higher for the more hydrophobic NPs at almost all values of Φ. Similar to Method 1, this may be attributed to the hydrophobic particles being more efficiently transferred

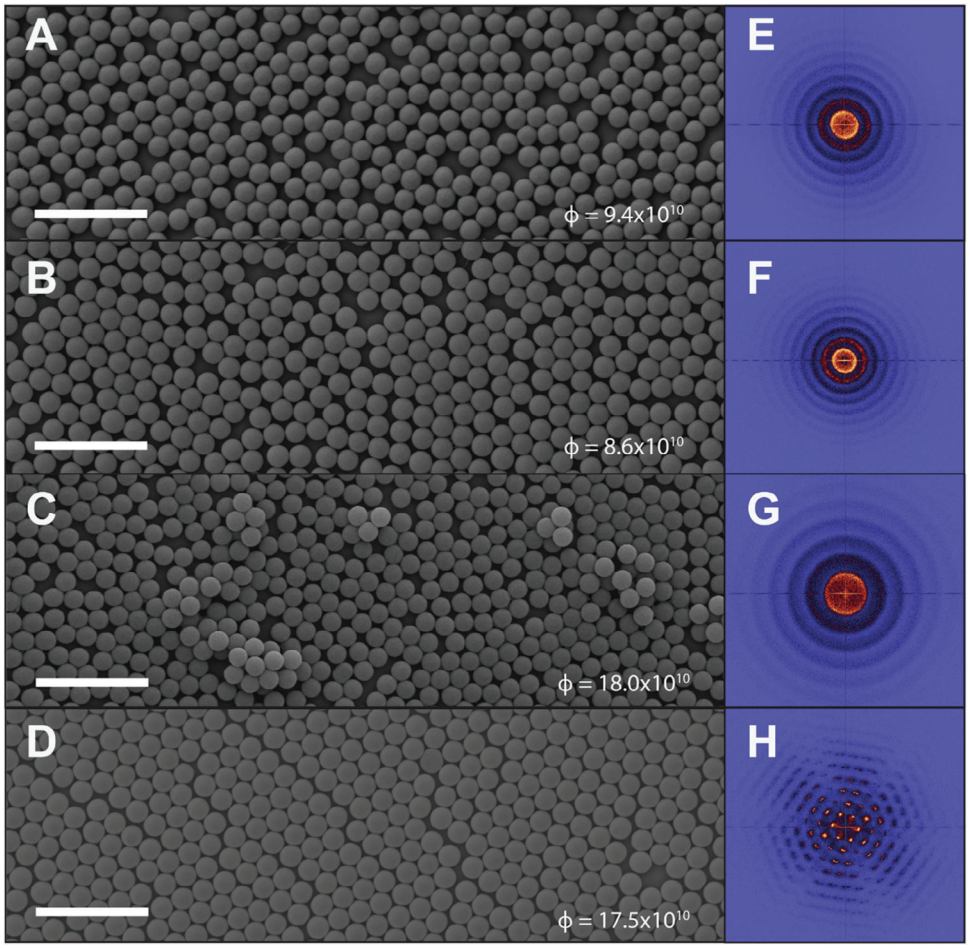


**Figure 3.** a–d) Scanning electron microscope (SEM) images of nanoparticle (NP) monolayers self-assembled via Method 2 at low Φ (a,b) and high Φ (c,d) and colloidal solutions with low $|\zeta|$ (a,c) and high $|\zeta|$ (b,d). Fourier transform of self-assembled NP monolayers prepared via Method 2 with $|\zeta|$ = 30 mV (e,g), $|\zeta|$ = 70 mV (f,h). All scale bars shown are 5 µm.

to the liquid interface as it is more energetically favorable for hydrophobic particles to occupy the liquid interface than the polar bulk water volume. Interestingly, the average self-assembly rates for high $|\zeta|$ solutions sharply diverge from the low $|\zeta|$ solutions at high NP concentrations ($\Phi = 13.9 \times 10^{10}$ NPs min$^{-1}$) and reaches a maximum average self-assembly rate of 181 cm$^2$ min$^{-1}$ ($\Phi = 17.5 \times 10^{10}$ NPs min$^{-1}$). All self-assembly rates presented in Figure 2c,d are averaged over five measurements. These results demonstrate a 142% increase in average monolayer self-assembly rate between high and low $|\zeta|$ solutions measured at the highest NP concentration when self-assembly is performed via Method 2. Notably, the fastest measured self-assembly rate for 1 µm PS NPs utilizing Method 2 was 268 cm$^2$ min$^{-1}$, consumed a total of 63.3 µL of NP solution, and formed a 169 cm$^2$ NP monolayer in 38 s. Additionally, under Method 2, the high $|\zeta|$ solutions average monolayer self-assembly rate show a nonlinear dependence on Φ for solutions with Φ > 8.61E10 NPs mL$^{-1}$. We attribute this rapid increase in monolayer self-assembly to attractive interparticle forces that arise from the high concentration of NPs in the micron sized dispensing droplets. Higher NP concentrations were not tested due to difficulties maintaining homogenously suspended NPs in the dispensing syringe which tended to show NPs settling along the syringe housing at higher NP concentrations.

As outlined in our previous work, attractive forces between NPs increase the probability that NPs are transferred to the air–water interface and prevent them from diffusing into the bulk water.[13] Therefore, as $n_{np}$ is increased each NP within a dispensing droplet can interact with a growing number of surrounding NPs which we believe explains the nonlinear increase in monolayer self-assembly rate observed in Method 2. From this argument it may be expected for low $|\zeta|$ solutions to have an even higher average monolayer self-assembly rate since attractive interparticle forces should be more pronounced for hydrophobic NPs. However, as will be shown, it is instead observed that low $|\zeta|$ solutions create large, irreversible NP aggregations which prevent long range ordering and lead to sedimentation of NPs into the bulk water volume.

**Figure 3** shows scanning electron microscope (SEM) images of 1 µm diameter PS NP monolayers self-assembled with via Method 2. Details of the sample preparation are described in Experimental Section. Figure 3a,b shows SEM images and Fourier transforms (Figure 3e,f) of self-assembled monolayers formed with low Φ. Interestingly, decreasing Φ does not lead to more

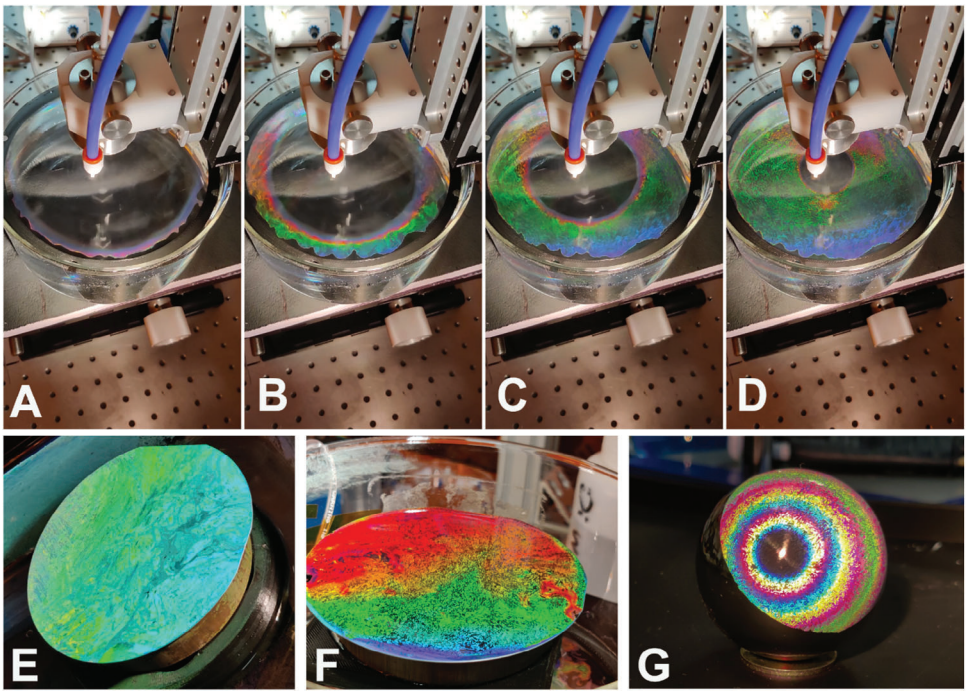


**Figure 4.** a–d) Photographs of aerosol assisted self-assembly Method 2 of 1 µm diameter polystyrene nanoparticles (NPs) on an air–water interface $t$ seconds after the start of deposition, a) $t = 2$ s, b) $t = 10$ s, c) $t = 20$ s, d) $t = 30$ s. e) Photograph of monolayer of 370 nm diameter polystyrene NPs transferred to a 4'' silicon wafer. Monolayer was prepared via Method 2. f) Photograph of monolayer of 750 nm diameter polystyrene NPs transferred to a 4'' silicon wafer. Monolayer was prepared via Method 2. g) Photograph of a 1 µm diameter polystyrene particle monolayer transferred to a reflective sphere (diameter = 7 cm). Before deposition the bottom half of the spherical substrate were masked off with Kapton tape to provide better contrast. Substrate preparation is further explained in Experimental Section.

ordered self-assembly of NP monolayers. It would be reasonable to assume that a dilute concentration of NPs may enable more uniform crystal self-assembly as this would decrease entropy in the local environment surrounding NPs. However, we instead observed that low $\Phi$ does not enable monolayer self-assembly with long-range order for NP solutions with a high $|\zeta|$ (Figure 3b,f) or low $|\zeta|$ (Figure 3a,e), although local order begins to develop for $|\zeta| = 70$ mV NP solutions (Figure 3b). Method 1 did not produce monolayers with long-range order under any deposition conditions. Photographs of monolayers self-assembled via Method 1 are shown in Figure S2 (Supporting Information).

Figure 3d shows that it is most favorable to form NP monolayers with long range order when NPs with a high $|\zeta|$ are introduced to the air–water interface under high NP concentration ($\Phi = 17.5 \times 10^{10}$ NP min$^{-1}$). When using high $|\zeta|$ solutions, this technique can readily form large single crystal domains (>2300 µm$^2$, Figure S3, Supporting Information) with minimal defects across a 158 cm$^2$ substrate area. Defects (point, line, aggregations, and grain boundaries) become significantly more pronounced as the $|\zeta|$ decreases (Figure 3a,c). Ultimately, this results in the loss of long-range order (Figure 3e,g) as the NPs become largely amorphously distributed. It was also confirmed that amorphous and ordered NP monolayers are formed at low and high $|\zeta|$, respectively, when stabilized with the cationic surfactant cetrimonium bromide (Figure S4, Supporting Information).

From these results we deduce that the large defect densities seen in low $|\zeta|$ NP monolayers arise from the decreased colloidal stability of the low $|\zeta|$ NPs. As outlined in Figure S5 (Supporting Information), when a new NP with a high $|\zeta|$ is introduced to a previously formed NP crystal (Figure S5a, Supporting Information) the NP transfers its momentum to the neighboring NPs via various scattering events (Figure S5b, Supporting Information). With a high $|\zeta|$, NPs are highly stable due to Coulombic repulsion; therefore, the disturbed NPs can dissipate the energy they acquired from the scattering event (Figure S5c, Supporting Information) without causing large aggregations. Additionally, when the atomized deposition is stopped, the surface tension gradient is lost and the liquid interface contracts, which allows the NPs to reassemble into a higher order configuration (Figure S5d, Supporting Information). However, for the case of low $|\zeta|$, the hydrophobic NPs will preferentially stick to each other when they interact with adjacent NPs after scattering events that are produced upon initial collision (Figure S5f, Supporting Information) and after the surface tension gradient is removed (Figure S5g, Supporting Information). This ultimately leads to a state of higher disorder (Figure S5h, Supporting Information) as irreversible NP aggregations are formed.

**Figure 4**a–d shows images of the real time monolayer self-assembly for 1 µm diameter polystyrene NPs self-assembled via Method 2 ($\zeta = -70$ mV, $\Phi = 17.5 \times 10^{10}$ NP min$^{-1}$) at 1 s (Figure 4a), 10 s (Figure 4b), 20 s (Figure 4c), and 30 s (Figure 4d) after the start of the aerosolized deposition. As shown, NPs travel radially away from the center of the retaining reservoir and accumulate on the circumference of the beaker where they continuously grow a NP monolayer. Grown monolayers are directly as-

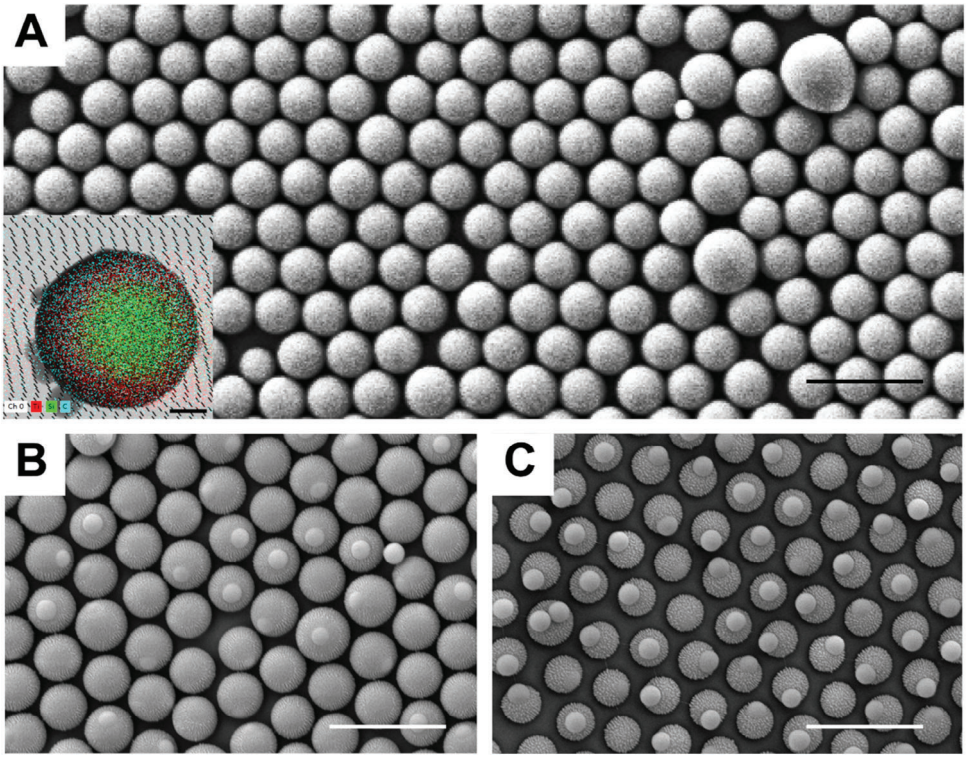


**Figure 5.** a) Scanning electron microscope (SEM) image of self-assembled core–shell SiO2@TiO2@PS nanoparticles (NPs) prepared via Method 2. b) SEM image of core–shell NPs from a) after 3 min of reactive ion etching in an O2 plasma. c) SEM image of core–shell NPs from a) after 5 min of etching in an O2 Plasma. Inset shows energy-dispersive X-ray (EDX) analysis of etched core–shell NPs from a) displaying the elemental signatures from silicon (green, core), titanium (red, inner shell), and carbon (blue, outer polymer shell). Inset scale bare is 100 nm. All other scale bars are 1.5 μm.

sembled into polycrystalline domains as evidenced by the strong specular iridescent reflection of the monolayer.

To confirm this technique's potential for use in a broad range of applications, the self-assembly of smaller diameter PS NPs, high refractive index core–shell NPs, and the transfer of self-assembled monolayers to curved substrates were tested. Figure 4e shows NP monolayers transferred to a four-inch silicon substrate made from 370 nm diameter SDS-stabilized PS NPs and 750 nm PS NPs (Figure 4f). In contrast to the high brightness and iridescence of the well-ordered monolayers self-assembled via Method 2, Figure S6 (Supporting Information) shows a photograph of a 1 μm PS NP monolayer transferred to a 4′ silicon wafer when prepared via Method 1. As shown, the amorphously arranged monolayer displays a noticeable decrease in brightness and iridescence. Lastly, a 1 μm PS NP monolayer was transferred to a 7 cm diameter reflective sphere (Figure 4g) to ascertain this self-assembly methods capacity to pattern nonflat substrates. Additional images of the self-assembly processes on the spherical substrate are provided in Figure S7 (Supporting Information). After transferring to the spherical substrate, the monolayer integrity and quality is well maintained. The ability to perform lithography or transfer submicron and subwavelength patterns onto nonflat substrates may be particularly important in developing the next generation of flexible and wearable electronics.

This technique can also be used to form well-ordered 2D monolayers of metal oxide NPs. SDS stabilized SiO2@TiO2@PS NPs were grown via emulsion polymerization with a SiO2 core diameter of 300 nm, TiO2 shell thickness of 25 nm, and a 100 nm thick PS outer shell. **Figure 5**a–c shows the TiO2 core–shell NPs after 0, 3, and 5 min of reactive ion etching in an O2 plasma. As shown, the core particles are not etched by the oxygen plasma, allowing them to be easily distinguished from the polymeric shell. The different layers of the core–shell NP can be clearly identified in the energy-dispersive X-ray (EDX) analysis of a single etched particle (Figure 5a inset). As expected, the elements characterizing the different shells (titanium and carbon) are found concentrically around the silicon oxide core. Monolayers grown from core–shell NPs show long range order (Figure S8a,b, Supporting Information); however nonideal synthesis of various larger diameter multicored NPs (Figure S8c–e, Supporting Information) affect the overall array crystallinity. Improved optimization of core–shell synthesis parameters or additional purification steps could be implemented to decrease the polydispersity of the aerosolizing solution. Various NP chemistries such as Au, SiO2, TiO2, and carbon are compatible with core–shell PS synthesis. By leveraging this platform, it may then be possible to form NP monolayers from heterogeneous materials and in nonclose packed geometries which is important to creating low-cost, colloidal analogs of dielectric and plasmonic metasurfaces.[11,53] Lastly, while large-area NP monolayer self-assembly has previously been demonstrated for colloidal Au and SiO2, the self-assembly methods have required the use of toxic, low-polarity solvents such as toluene and chloroform which are not compatible with various biological media.[29,32,33,40] As shown, by growing a thin polymer shell

over the metal oxide NPs, ethanol can continue to be used as the spreading agent, enabling development of biocompatible sensing applications.

In conclusion, we have demonstrated and characterized a novel self-assembly platform utilized for the high-throughput generation of high-quality submicron NP monolayers on an air–water interface. The method presented is simple, easy to implement, and parallelizable. To the best of our knowledge, this is the fastest monolayer self-assembly rate of any reported method. With optimized atomization conditions and NP surface chemistry, monolayer self-assembly rates as high as 268 $cm^2$ $min^{-1}$ are observed and constitute a 93× increase in monolayer self-assembly rate from previously reported rapid, high throughput NP self-assembly methods when normalized to a single injection source.[28] Monolayer formation rates using the technique reported here could be further increased by using multiple atomization sources in parallel. Similarly, this method demonstrates extremely efficient transfer of NPs to the air–water interface (Figure S9, Supporting Information) and reduces the amount of consumed NP solution per unit area of monolayer formed by 13.4×.[28] Compared to standard LB methods, which operate on the 1–10′s $mm^2$ $min^{-1}$ range, we achieve a three to four order-of-magnitude increase in monolayer self-assembly rate. New physical descriptions outlining the mechanisms enabling the improved self-assembly rates dependence on $|\zeta|$ are described and analyzed. Additionally, these insights were leveraged to self-assemble monolayers of multilayered high-index core–shell NP arrays. We anticipate that this platform will enable highly cost-effective submicron lithography due to its high-volume throughput, highly efficient transfer of NPs to the air–water interface, and broad applicability to NPs of various sizes and materials. With the physical insights provided, this work can also further the theoretical understanding of NP crystallization and help create novel new NP metasurfaces which may benefit from the large manufacturing throughput and the ability to co-assemble heterogeneous NP mixtures.

## 3. Experimental Section

*Materials*: Styrene (SKU: 807679), potassium persulfate (KPS, SKU: 216224), sodium dodecyl sulfate (SDS, SKU: 8.17034), sodium chloride (NaCl, SKU: S5886), 200 Proof Anhydrous Ethanol (SKU: 459844), 2,2′-azobis(2-methylpropionamidine) dihydrochloride (AIBA, SKU: 440914), tetraethyl orthosilicate (TEOS, SKU: 8.00658), ammonia solution-25% in water (SKU: 1.05428), activated basic aluminum oxide (SKU: 199443), and 3-(trimethoxysily)propyl methacrylate (MPS, SKU: 440159) were purchased from Sigma–Aldrich—chemical acronyms and product numbers are provided. High purity deionized (DI) water with resistivity 18 MΩ cm was used in preparation of any mentioned aqueous solutions and provided by in house facilities. All chemicals were used as is and without any further purification unless otherwise specified.

*Nanomicroparticle Synthesis*: To prepare monodisperse polystyrene microparticles, styrene monomer was first filtered to remove polymerization inhibitors. A chromatography column was prepared with moderately packed glass wool and basic aluminum oxide. Styrene monomer was carefully poured into the chromatography column and filtered through the basic alumina. Purified styrene was sealed and stored in a refrigerator for further use. Polystyrene microparticles were synthesized via emulsion polymerization. For a typical synthesis of 1 µm diameter polystyrene microparticles, 110 mL of ethanol, 40 mL of DI water, and 15 mL of purified styrene were combined in a 250 mL three neck flask. NaCl (0.075 g) and SDS (0.205 g) were added to the styrene solution. The three-neck flask was sealed, attached to a condensing column, and placed on a magnetic stirring plate. The styrene solution was purged with N2 gas for 30 min and stirred at 400 rpm. After purging, the styrene solution was raised to 70 °C and left to equilibrate for 1 h. Lastly, 4 mL of 0.025 g $mL^{-1}$ (KPS in water) was added to begin the reaction. After 24 h, the solution was collected and centrifuged at 8K RPM for 10 min to remove residual synthesis reagents. Low $|\zeta|$ solutions were centrifuged three times in ethanol to desorb stabilizing surfactants (SDS or cationic surfactant cetrimonium bromide). High $|\zeta|$ solutions were washed three times in DI water. Smaller polystyrene particles were made under the same conditions using smaller quantities of styrene and/or higher reaction temperatures.

*Core–Shell Particle Synthesis*: To prepare the SiO2@TiO2 particles, 0.09 g of silica spheres were dispersed in a mixture of 100 mL of ethanol and 0.30 mL of ammonia hydroxide (28 wt%). The solution was then ultrasonicated for 20 min and the temperature raised to 45 °C. Afterwards, 0.75 mL of titanium butoxide was added dropwise within 3 min and the reaction was mechanically stirred using a magnetic stirrer. After 24 h, the solution was washed three times with ethanol and DI water and resuspended in 20 mL of ethanol.[54] 5 mL of MPS was then added into the SiO2@TiO2 solution and mixed for 48 h. The SiO2@TiO2 solution was then cleaned with ethanol three times and redispersed in 2 mL of ethanol. Afterwards, the SiO2@TiO2 particles were dispersed in 32 mL of ethanol and water mixture; ethanol/water:7/3. After degassing the solution with N2 for 30 min, 1 mL of styrene was added to the system and the temperature raised to 75 °C. Once the desired temperature was reached, 1.0 ml of 2.0 wt % KPS (aqueous) was injected to initiate the polymerization process. Twenty hours later, the SiO2@TiO2@PS core–shell particles were separated via centrifugation and cleaned with ethanol three times.

*Nanomicroparticle Aerosol Solution*: To prepare the aerosolized NP solutions the triple washed particle solutions were mixed into a 15 mL centrifuge tube in a 1:1 ratio of pure ethanol and DI water. Microparticle spray solutions were sonicated for 15 min at and vortexed for 5 min at prior to use to ensure NPs were fully resuspended. The concentration of NPs in the atomizing solution was determined by decanting 1 mL into a 20 mL glass vial and annealing at 80 °C for 3 h. The mass of the dried NPs was recorded and used to calculate the NP concentration. Lower concentration spray solutions were prepared from dilutions of a high concentration stock solution.

*Aerosolized NP Monolayer Self-Assembly*: A home built computer-controlled system was used to trigger an atomizing AccuMist nozzle (120 KHz, Sono-Tek) affixed to a *Z*-axis translation stage mounted onto a *XY* gantry. NP solutions were delivered to the atomizing nozzle via a programmable syringe pump (Sono-Tek). Dry air was used for air-shaping of the atomized beam and was maintained below 1 PSI. Nozzle power, fluid flow rate, air pressure, ultrasonic signal generation, and valve timing and triggering were controlled via an Arduino Mega communicating with an ALIGN Precision Ultrasonic Spray Platform System (Sono-Tek).

In a typical spray coat, a 16.5 cm diameter crystallization dish was filled with 1.5 L of DI water. A 2 mm thick (16.2 cm outer diameter, 14.6 cm inner diameter) retaining ring was 3D printed from a spool of polyactic acid filament (Hatchbox) and placed on the air–water interface to prevent the self-assembled monolayer from sticking to the glass sidewalls. The nozzle head was centered over the crystallization dish and placed 40 mm above the air–water interface. To begin spray coating a trigger signal was sent to the ultrasonic nozzle, syringe pump, air valve, and timer to begin simultaneously. Spray coating was stopped manually when the air–water interface was saturated with the NP monolayer which was easily visually recognized in a procedure outlined by Menath et. al.[52] The bulk water volume was then pumped out of the crystallization dish with a peristaltic pump which transferred the self-assembled NP monolayer to the substrate of interest. Silicon substrates were cleaned with acetone followed by ethanol before deposition. Spherical substrates were precleaned with ethanol and soapy water. The bottom half of spherical substrates were then masked off with Kapton tape to provide contrast. All self-assemblies were performed at 120 KHz atomizing nozzle frequency, 1.5 W nozzle power, 0.1 mL $min^{-1}$ fluid delivery rate, and 1.0 PSI unless otherwise specified.

*Scanning Electron Microscopy*: High resolution electron microscopy and EDX spectroscopy were performed with a ZEISS Neon 40EsB system.

When collecting SEM images samples were first coated with ≈4 nm of gold via a benchtop sputter coated. EDX samples were not precoated.

*Zeta-Potential Measurements*: The zeta potential of polystyrene and silica spheres was measured using a Malvern Zetasizer Nano ZS. All reported zeta potential measurements were done with a 0.03 wt% concentration of NPs.

## Supporting Information

Supporting Information is available from the Wiley Online Library or from the author.

## Acknowledgements

G.C. and E.Y. conceived the idea and designed the experiments. R.B. conducted and led the colloidal particle synthesis and characterizations. G.C. and R.B. contributed equally to this work. All authors discussed the results and commented on the manuscript. This work was primarily supported by The Center for Dynamics and Control of Materials (CDCM) under National Science Foundation award numbers DMR-1720595 and DMR-2308817. This work was performed in part at the University of Texas at Austin's Microelectronics Research Center, a member of the National Nanotechnology Coordinated Infrastructure (NNCI), which is supported by the National Science Foundation grant (grants ECCS-1542159 and ECCS-2025227). This research was partially supported by the U.S. National Science Foundation through Award #1828974 and the Robert A. Welch Foundation (Grant F-1464).

## Conflict of Interest

A provisional patent application incorporating developments reported here has been submitted.

## Data Availability Statement

The data that support the findings of this study are available from the corresponding author upon reasonable request.

## Keywords

colloids, metasurfaces, monolayer, nanolithography, nanopatterning, self-assembly

Received: September 20, 2023
Revised: November 1, 2023
Published online:

[1] M. Yamaguchi, T. Masuda, K. Araki, D. Sato, K.-H. Lee, N. Kojima, T. Takamoto, K. Okumura, A. Satou, K. Yamada, T. Nakado, Y. Zushi, Y. Ohshita, M. Yamazaki, *Prog. Photovoltaics* **2021**, *29*, 684.
[2] M. L. Tseng, Y. Jahani, A. Leitis, H. Altug, *ACS Photonics* **2021**, *8*, 47.
[3] T. Abdelfatah, M. Jalali, S. G. Yedire, I. I. Hosseini, C. Del Real Mata, H. Khan, S. V. Hamidi, O. Jeanne, R. Siavash Moakhar, M. Mclean, D. Patel, Z. Wang, G. Mckay, M. Yousefi, D. Nguyen, S. M. Vidal, C. Liang, S. Mahshid, *Nat. Nanotechnol.* **2023**, *18*, 922.
[4] L. Yuan, A. Kuriakose, J. Zhou, H. Robatjazi, P. Nordlander, N. J. Halas, *J. Phys. Chem. C* **2022**, *126*, 13714.
[5] E. Shirman, T. Shirman, A. V. Shneidman, A. Grinthal, K. R. Phillips, H. Whelan, E. Bulger, M. Abramovitch, J. Patil, R. Nevarez, J. Aizenberg, *Adv. Funct. Mater.* **2018**, *28*, 1704559.
[6] J. Buencuerpo, T. E. Saenz, M. Steger, M. Young, E. L. Warren, J. F. Geisz, M. A. Steiner, A. C. Tamboli, *Nano Energy* **2022**, *96*, 107080.
[7] D. Cardwell, A. Kirk, C. Stender, A. Wibowo, F. Tuminello, M. Drees, R. Chan, M. Osowski, N. Pan, *2017 IEEE 44th Photovoltaic Specialist Conference (PVSC)*, IEEE, Piscataway, NJ **2017**, p. 3511, https://doi.org/10.1109/PVSC.2017.8366552.
[8] M. O. Reese, S. Glynn, M. D. Kempe, D. L. Mcgott, M. S. Dabney, T. M. Barnes, S. Booth, D. Feldman, N. M. Haegel, *Nat. Energy* **2018**, *3*, 1002.
[9] I. Massiot, A. Cattoni, S. Collin, *Nat. Energy* **2020**, *5*, 959.
[10] B. I. Karawdeniya, A. M. Damry, K. Murugappan, S. Manjunath, Y. M. N. D. Y. Bandara, C. J. Jackson, A. Tricoli, D. Neshev, *Chem. Rev.* **2022**, *122*, 14990.
[11] A. E. Miroshnichenko, Y. S. Kivshar, *Nano Lett.* **2012**, *12*, 6459.
[12] W. Jiang, B. Q. L. Low, R. Long, J. Low, H. Loh, K. Y. Tang, C. H. T. Chai, H. Zhu, H. Zhu, Z. Li, X. J. Loh, Y. Xiong, E. Ye, *ACS Nano* **2023**, *17*, 4193.
[13] G. Cossio, E. T. Yu, *Nano Lett.* **2020**, *20*, 5090.
[14] G. Cossio, E. Yu, R. Tatavarti, B. Scandrett, E. Yu, *IEEE J. Photovoltaics* **2021**, *11*, 685.
[15] J. Zhu, Z. Yu, G. F. Burkhard, C.-M. Hsu, S. T. Connor, Y. Xu, Q. Wang, M. Mcgehee, S. Fan, Y. Cui, *Nano Lett.* **2009**, *9*, 279.
[16] A. Rahman, A. Ashraf, H. Xin, X. Tong, P. Sutter, M. D. Eisaman, C. T. Black, *Nat. Commun.* **2015**, *6*, 5963.
[17] B. M. Gawlik, G. Cossio, H. Kwon, Z. Jurado, B. Palacios, S. Singhal, A. Alù, E. T. Yu, S. V. Sreenivasan, *Opt. Express* **2018**, *26*, 30952.
[18] J.-G. Park, S.-H. Kim, S. Magkiriadou, T. M. Choi, Y.-S. Kim, V. N. Manoharan, *Angew. Chem., Int. Ed.* **2014**, *53*, 2899.
[19] F. Sterl, E. Herkert, S. Both, T. Weiss, H. Giessen, *ACS Nano* **2021**, *15*, 10318.
[20] Z. Dong, J. Ho, Y. F. Yu, Y. H. Fu, R. Paniagua-Dominguez, S. Wang, A. I. Kuznetsov, J. K. W. Yang, *Nano Lett.* **2017**, *17*, 7620.
[21] P. Liu, L. Bai, J. Yang, H. Gu, Q. Zhong, Z. Xie, Z. Gu, *Nanoscale Adv* **2019**, *1*, 1672.
[22] K. Vynck, R. Pacanowski, A. Agreda, A. Dufay, X. Granier, P. Lalanne, *Nat. Mater.* **2022**, *21*, 1035.
[23] T. Qiu, E. M. Akinoglu, B. Luo, M. Konarova, J.-H. Yun, I. R. Gentle, L. Wang, *Adv. Mater.* **2022**, *34*, 2103842.
[24] S.-H. Wu, G. Cossio, B. Braun, F. C. M. Wu, E. T. Yu, *Adv. Opt. Mater.* **2023**, *11*, 2202409.
[25] C. L. Haynes, R. P. Van Duyne, *J. Phys. Chem. B* **2001**, *105*, 5599.
[26] H. W. Deckman, J. H. Dunsmuir, *Appl. Phys. Lett.* **1982**, *41*, 377.
[27] Hulteen, J. C., R. P. Van Duyne, *J. Vac. Sci. Technol., A* **1995**, *13*, 1553.
[28] P. Gao, J. He, S. Zhou, X. Yang, S. Li, J. Sheng, D. Wang, T. Yu, J. Ye, Y. Cui, *Nano Lett.* **2015**, *15*, 4591.
[29] T. Kohoutek, M. Parchine, M. Bardosova, M. E. Pemble, *Colloids Surf. A* **2020**, *593*, 124625.
[30] E. Sirotkin, J. D. Apweiler, F. Y. Ogrin, *Langmuir* **2010**, *26*, 10677.
[31] N. Vogel, S. Goerres, K. Landfester, C. K. Weiss, *Macromol. Chem. Phys.* **2011**, *212*, 1719.
[32] V. Lotito, T. Zambelli, *Adv. Colloid Interface Sci.* **2017**, *246*, 217.
[33] J.-Y. Choi, T. L. Alford, C. B. Honsberg, *Langmuir* **2014**, *30*, 5732.
[34] B. G. Prevo, O. D. Velev, *Langmuir* **2004**, *20*, 2099.
[35] N. Arai, S. Watanabe, M. T. Miyahara, *Langmuir* **2019**, *35*, 11533.
[36] S. Jeong, L. Hu, H. R. Lee, E. Garnett, J. W. Choi, Y. Cui, *Nano Lett.* **2010**, *10*, 2989.
[37] M. Parchine, J. Mcgrath, M. Bardosova, M. E. Pemble, *Langmuir* **2016**, *32*, 5862.
[38] X. Li, J. F. Gilchrist, *Langmuir* **2016**, *32*, 1220.
[39] H.-L. Nie, X. Dou, Z. Tang, H. D. Jang, J. Huang, *J. Am. Chem. Soc.* **2015**, *137*, 10683.
[40] I.-T. Chen, E. Schappell, X. Zhang, C.-H. Chang, *Microsyst. Nanoeng.* **2020**, *6*, 22.

[41] M. Rey, T. Yu, K. Bley, K. Landfester, D. M. A. Buzza, N. Vogel, *Langmuir* **2018**, *34*, 9990.
[42] H. Kim, K. Muller, O. Shardt, S. Afkhami, H. A. Stone, *Nat. Phys.* **2017**, *13*, 1105.
[43] A. Mahajan, C. D. Frisbie, L. F. Francis, *ACS Appl. Mater. Interfaces* **2013**, *5*, 4856.
[44] M. S. Saleh, C. Hu, R. Panat, *Sci. Adv.* **2017**, *3*, e1601986.
[45] X. Chen, J. M. Lawrence, L. T. Wey, L. Schertel, Q. Jing, S. Vignolini, C. J. Howe, S. Kar-Narayan, J. Z. Zhang, *Nat. Mater.* **2022**, *21*, 811.
[46] J. H. Bang, R. J. Helmich, K. S. Suslick, *Adv. Mater.* **2008**, *20*, 2599.
[47] N. J. Wilkinson, M. A. A. Smith, R. W. Kay, R. A. Harris, *Int. J. Adv. Manuf. Technol.* **2019**, *105*, 4599.
[48] H. Kim, J. Lee, T.-H. Kim, H.-Y. Kim, *Langmuir* **2015**, *31*, 8726.
[49] A. Saha, Y. Wei, X. Tang, C. K. Law, *J. Fluid Mech.* **2019**, *875*, 842.
[50] F. Jia, K. Sun, P. Zhang, C. Yin, T. Wang, *Phys. Rev. E: Stat. Phys., Plasmas, Fluids, Relat. Interdiscip. Top.* **2020**, *5*, 073605.
[51] F. K. A. Gregson, M. Ordoubadi, R. E. H. Miles, A. E. Haddrell, D. Barona, D. Lewis, T. Church, R. Vehring, J. P. Reid, *Phys. Chem. Chem. Phys.* **2019**, *21*, 9709.
[52] J. Menath, R. Mohammadi, J. C. Grauer, C. Deters, M. Böhm, B. Liebchen, L. M. C. Janssen, H. Löwen, N. Vogel, *Adv. Mater.* **2023**, *35*, 2206593.
[53] J. A. Fan, C. Wu, K. Bao, J. Bao, R. Bardhan, N. J. Halas, V. N. Manoharan, P. Nordlander, G. Shvets, F. Capasso, *Science* **2010**, *328*, 1135.
[54] W. Li, J. Yang, Z. Wu, J. Wang, B. Li, S. Feng, Y. Deng, F. Zhang, D. Zhao, *J. Am. Chem. Soc.* **2012**, *134*, 11864.